Graphical Abstract

Unifying stability and plasmonic properties in hybrid nanoislands: Au-Ag synergistic effects and application in SERS

Matej Bubaš, Ivana Fabijanić, Adriana Kenđel, Snežana Miljanić, Maria Chiara Spadaro, Jordi Arbiol, Vesna Janicki, Jordi Sancho-Parramon

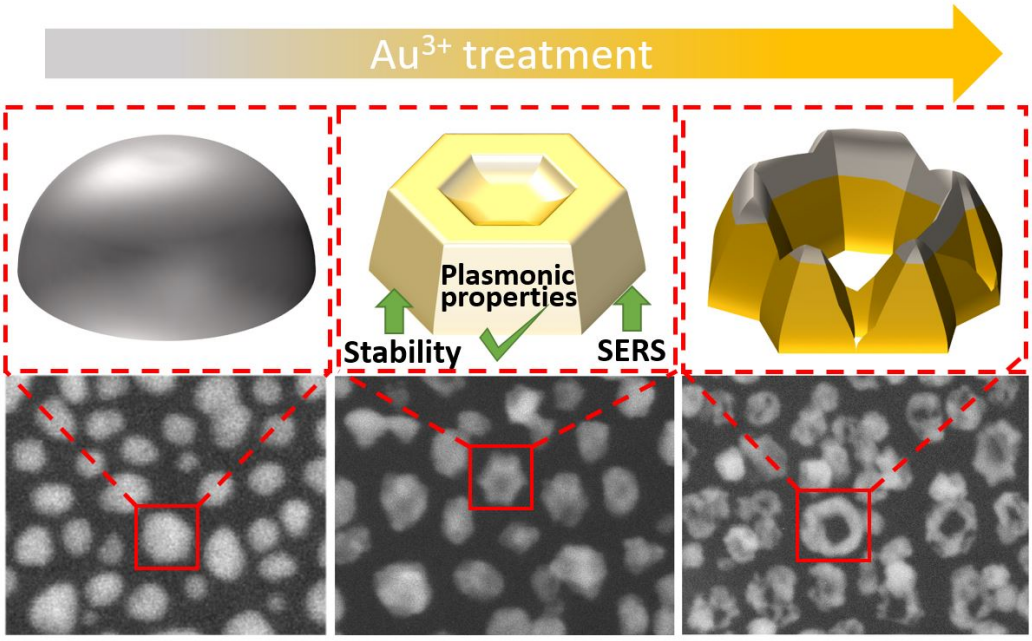

Highlights

Unifying stability and plasmonic properties in hybrid nanoislands: Au-Ag synergistic effects and application in SERS

Matej Bubaš, Ivana Fabijanić, Adriana Kenđel, Snežana Miljanić, Maria Chiara Spadaro, Jordi Arbiol, Vesna Janicki, Jordi Sancho-Parramon

- Wide plasmon tunability achieved by galvanic replacement of Ag with Au
- Conditions to obtain islands with Ag-like plasmons but far better stability are found
- Nanoislands with increased stability also showed best SERS detection performance
- DFT and electrodynamics simulations provided key insights on the observed behaviour

Unifying stability and plasmonic properties in hybrid nanoislands: Au-Ag synergistic effects and application in SERS

Matej Bubaš[a], Ivana Fabijanić[a], Adriana Kenđel[b], Snežana Miljanić[b], Maria Chiara Spadaro[c,d], Jordi Arbiol[c,d], Vesna Janicki[a], Jordi Sancho-Parramon[a,*]

[a] *Ruđer Bošković Institute, Bijenička cesta 54, Zagreb 10000, Croatia*
[b] *University of Zagreb, Faculty of Science, Horvatovac 102a, 10000 Zagreb, Croatia*
[c] *Catalan Institute of Nanoscience and Nanotechnology (ICN2), CSIC and BIST, Campus UAB, Bellaterra, 08193 Barcelona, Catalonia, Spain*
[d] *ICREA, Pg. Lluís Companys 23, 08010 Barcelona, Catalonia, Spain*

Abstract

In plasmon-based devices, the choice of metal for the nanostructures often leads to an undesirable tradeoff between either superb performance of Ag or stability of Au. There is a great interest in combining Au and Ag in a way that preserves both their favourable properties, while also exploiting synergistic effects to boost surface-enhanced Raman scattering (SERS) performance beyond the capabilities of a single metal. To address this issue, large-area nanofabrication procedure based on galvanic replacement was used to create hybrid Au-Ag nanoislands with a diverse morphology and highly tunable (through visible to NIR) plasmon resonance. Their stability was comprehensively studied and shown to be complex to achieve. However, in the right conditions, Au-Ag nanoislands with silver-like plasmonic properties were fabricated, and shown to be stable over a period of at least 5 months. Moreover, their SERS efficiency considerably outperformed even that of Ag nanoislands. Computational investigation helped explain the advantageous properties and provided insights for future sensor design. Detection of the model molecules was achieved in the nanomolar range and in mild conditions (low laser power), indicating great potential for biomedicine sensing. Beyond

*Corresponding author
Email address: jsancho@irb.hr (Jordi Sancho-Parramon)

Version accepted for publication in Sensors and Actuators B: Chemical

that, nanoislands with simultaneous stability and good plasmonic properties can find application in a wide variety of photonic devices.

Keywords: plasmonics, hybrid nanoislands, alloys, galvanic replacement, stability

---

1. Introduction

In the last couple of years, the field of plasmonics has reached a tipping point, transforming from the field with a lot of potential to the field bringing major innovations to practical use. Several different research areas utilizing plasmonic metal nanoparticles, such as photothermal cancer treatment [1], solar energy harvesting, [2, 3] and green chemistry photocatalysis [4] have almost simultaneously reached the verge of commercialization, while plasmon-based sensing leads the way with recently established commercial applications [5]. Plasmon-based sensing has shown to be especially important for biomedical use, playing a pivotal role in the widespread rapid virus detection in a recent global pandemic situation, utilizing gold nanoparticles [6, 7, 8]. Along with the gold nanoparticles, silver nanoparticles have found widespread use, especially in surface-enhanced Raman spectroscopy (SERS) due to the larger electric field enhancement, which results in stronger Raman scattering and improved sensor performance. [9]

However, lower chemical resistance of silver nanoparticles presents a significant drawback since, for practical purposes, stability and longevity are of paramount importance. [9, 10, 11] In fact, along with larger field enhancement, silver nanoparticles exhibit almost universally better plasmonic properties when compared to gold ones, such as higher extinction cross sections, larger resonance quality factors and lower optical losses. [9, 12, 13, 14] Thus, the interplay between chemical stability and plasmonic properties is critical in the choice of nanoparticle material, which usually requires compromises.

This issue is particularly prominent in SERS where both properties carry great importance. Recently, the potential of gold/silver alloy nanostructures for SERS has been highlighted due to the possible synergistic properties of the metal combination [15, 16, 17, 18], while (non-alloyed) hybrid metal nanostructures have also shown improvement of SERS performance [19, 20, 21]. Moreover, by tuning the localized surface plasmon resonance (LSPR) with the use of bimetallic nanostructures, the conditions for SERS-based detection of chromophores can be optimized [22, 23, 24].

Alongside gold and silver, many other transition metals [25, 26, 21] and semiconductors [27, 28] have been tested as active substrates for SERS. However, only good plasmonic metals such as copper, silver, and gold have shown the outstanding SERS performance due to large field enhancement. Since field enhancement is a crucial parameter for SERS performance, a lot of research has been directed towards modifying nanostructures to optimize performance. There is evidence that increasing the size of nanoparticle can be beneficial [29], although adding smaller nanoparticles to lower the interparticle distance seems to significantly improve the performance due to increased field enhancement between particles [30]. Careful isolation of the influence of nanoparticle distance on the field enhancement shows a substantial increase of the field between the particles as the gap size decreases below 50 nm. [31] Finally, research on the influence of nanostructure shape on the SERS performance points to beneficial properties of sharp edges and high aspect ratio features. [32, 33, 34, 35] Control of these parameters varies in different fabrication approaches, with sophisticated and expensive lithography usually providing the highest degree of control. However, due to low cost and ease of fabrication, nanoparticle suspensions in solution, or assemblies on the surface, provide a competitive alternative for industrial applications, especially with recent advances in morphology control. [36, 37, 38]

In this work we present a straightforward procedure based on the galvanic replacement of silver with gold, suitable for large-area nanofabrication and allowing for a high degree of mophological tunability. It enables the creation of nanoislands with composition and morphology varying from fully alloyed nanoislands to clusters of nanorings with core-shell structures. As a result, their plasmon resonance can be deliberately tuned through the whole visible range, and extended well into the near-infrared window - the wavelength range where light has the largest penetration depth into the biological tissue. [39] The obtained hybrid metal nanostructures are appropriate for SERS, especially of sensitive samples, as they enable the detection of model molecules in the nanomolar range at extremely low laser power. Furthermore, we highlight the importance of ageing measurements to assess the practical applicability of the produced nanostructures. Based on the results of ageing measurements, we are able to identify the treatment conditions that produce islands with the highest stability - a key property for any type of sensing. Using density functional theory calculations, we show that charge transfer effects from Ag to Au contribute to the excellent stability of Ag-Au alloyed nanoislands. Despite good chemical resistance, we demonstrate that

the plasmonic properties can sometimes continue to change even in very mild conditions, and attribute that effect to morphological changes.

The results obtained by extensive morphological, compositonal and optical characterization, as well as SERS potency of the samples, point to the fabricated nanoislands that exhibit the combination of the highest stability, best SERS performance, and excellent plasmonic properties. High-throughput fabrication of nanoislands with gold-like stability and silver-like plasmonic properties could prove to be important beyond sensing capabilities, carrying a large potential in the field of plasmonics in general.

2. Methods

The method for sample preparation was based on the method outlined by Fabijanić et al [40] but includes several modifications. The sample preparation workflow is shown in the figure S14.

Evaporation

The first step in the sample preparation was Ag deposition on glass substrates (Menzel) by electron beam evaporation in a modified Varian chamber. The base pressure was set to 10^{-6} torr and the deposition rate was set to approximately 1 Å/s. For the deposition, the substrates were preheated at 200 ℃. The preheating is done to ensure the growth of the film in the form of separated nanoislands.

Annealing

After the deposition, the samples were annealed in air at 300 ℃ for 1h, to enhance island formation, uniformity and sphericity. After the heating was stopped, the annealing chamber was not opened and the samples were left to slowly cool until the next day. Slow cooling was shown to improve the adhesion of the thin film of metal nanoislands to the glass substrate which results in less island desorption and flaking, better homogeneity and overall improved preservation of the samples after chemical treatment. The effect of slow cooling versus quick quenching after otherwise identical annealing conditions is shown in the Figure S1.

Chemical treatment/galvanic replacement

The galvanic replacement was performed in a stepwise manner, with the number of identical steps controlling the reaction progression.

One step consists of first adding 25 mL of milli Q water (MQW, 18 MΩ com-1) preheated to 90 ℃ in a 50 mL beaker, placed on a magnetic stirrer, containing a Teflon grid as a sample holder, and a magnetic rod underneath

the holder. The preheating was done to avoid solid $AgCl_3$ formation on the surface of the sample. Next, 150 µL aliquot of 2mM aqueous solution of $HAuCl_4$ is added in the beaker and stirred for 30 s at 1500 rpm. Immediately after, the sample is immersed in the solution and removed after 1 min. Upon removal from the solution, the sample is thoroughly rinsed with ethanol (HPLC grade, Sigma-Aldrich) and air-dried.

The steps described above were repeated until the desired total reagent volume has been reached. The exception was made for samples treated with 350 µL, with the volume of the $HAuCl_4$ aliquot changed to 100 µL in the first two steps, because the desired total volume was not divisible by 150 µL.

UV/Vis spectroscopy

Transmission measurements were done in the spectral range from 200 - 1100 nm. using a UV/Vis Lambda 25 Perkin Elmer spectrophotometer equipped with deuterium and halogen lamps.

Ellipsometry

To complement the transmission measurements, optical properties were further investigated by spectroscopic ellipsometry, using a J. A. Woollam V-Vase ellipsometer. A larger spectral range (0.57 - 5 eV, or approximately 248 - 2175 nm) was used. The measurements were performed at angles of incidence of 55°, 65° and 75°. Modeling of the thin metal nanoisland film effective optical constants was performed using a flexible multiple-oscillator model with gaussian oscillators, to account for localized surface plasmon resonance and interband transitions of nanoparticles with varying compositions, shapes, sizes, and interparticle distances. Uncoated substrates were also characterized by ellipsometry with the optical constants obtained by a point-by-point fitting.

Scanning electron microscopy (SEM)

Scanning electron microscopy (SEM) measurements were done to connect the insights obtained by optical measurements with the sample morphology. Plain view images were taken using a field-emission microscope Jeol JSM 7000F at an acceleration voltage of 1 kV. Surface elemental analysis was done by energy dispersive spectroscopy (EDS) with a EDS/INCA 350 (energy dispersive X-ray analyzer) unit linked to the microscope.

Transmission electron microscopy (TEM)

Further structural and morphological insights were obtained by scanning transmission electron microscopy (STEM) performed on a field emission gun FEI Tecnai F20 microscope. The combination of high angle annular dark-field (HAADF) STEM, and the electron energy loss spectroscopy (EELS)

performed in the Tecnai microscope by using a GATAN QUANTUM filter, was used to obtain compositional maps. For EELS mapping of C, K-edge at 284 eV was used, M4,5-edges at 367 eV was used for Ag and M4,5-edge at 2206 eV for Au.

Surface-enhanced Raman scattering (SERS)

To test the SERS efficiency of the prepared nanostructures 4-aminothiophenol (4-ATP) and rhodamine 6G (R6G) were used as model molecules. Solutions of model molecules, c = 1×10^{-5} M, were prepared by dissolution of R6G and 4-ATP in Milli-Q water and methanol/Milli-Q water mixture (1% v/v), respectively, while solutions of lower concentrations (1×10^{-6} M, 1×10^{-7} M, 1×10^{-8} M) were obtained by dilution of 1×10^{-5} M solution with Milli-Q water. Samples for SERS measurements were prepared by applying 1 µL of an appropriate 4-ATP or R6G solution on the metallic substrate and the formed drop was left to dry. Raman and SERS spectra were measured on a Renishaw inVia Raman microscope equipped with a laser emitting at 785 nm and 532 nm. Raman spectra of the solid compounds were recorded on an aluminum holder using ×5 objective (NA = 0.12), while the SERS spectra of the compounds on the metallic substrates were acquired using ×20 objective (NA = 0.40). For all the samples spectra were taken with 10-s exposure time and one accumulation, except for the solid R6G sample, in which case five accumulations were collected for a spectrum. The applied laser power depended on the sample. Hence, the Raman spectrum of solid 4-ATP was obtained at the laser power of 16 mW, while the SERS measurements of 4-ATP samples were performed using the laser power of 0.1 mW. Due to strong fluorescence of R6G, the Raman spectrum of the solid substance was acquired at 0.0003 mW, while the SERS spectra of R6G samples were measured using 0.2 mW laser power. For each SERS sample, the spectra were taken in triplicate and the averaged spectrum was shown in figures. The raw spectra were baseline corrected using the WiRE 5.3 software.

Electrodynamics simulations

Electromagnetic response of a core-shell particle is computed using the Mie theory extension developed by Aden and Kerker [41]. In essence, all the involved electromagnetic fields (incident, scattered and those in the shell and in the core) are expanded in terms of vector spherical harmonics that represent multipole electric and magnetic fields. Imposing boundary conditions at the interfaces of the particle (core-shell and shell-external medium) the expansion coefficients can be determined and relevant far-field and near-field quantities can be computed. Otical constants of materials for simulations

were taken from [42].

In the case of particle clusters, calculations are based in the generalized multiparticle Mie theory [43]. Like in the previous case, incident, scattered and internal fields are expanded in a series of vector spherical harmonics defined with respect to the center of the particle. The field acting over each particle is the sum of the incident field and the field scattered by all other particles. Imposing boundary conditions at every particle surfaces, a linear system connecting the scattered and incident field expansion coefficient results. The system of equations is truncated to a maximum multipolar degree (typically around 5) until convergence of the computed far field or near field quantities is reached.

Density Functional Theory (DFT) calculations

Density functional theory calculations were performed using the GPAW package. [44, 45] It is based on projector augmented wave (PAW) method and utilizes the atomic simulation environment (ASE). [46] Since the periodic boundary conditions were used for system modelling, the basis set was constructed using plane waves. Monkhorst-Pack grid [47] was used for Brilluin zone sampling, and occupation number smearing was of Fermi-Dirac type with 0.1 eV width.

A 4 layer slab of Ag-Au alloy with 3 to 1 ratio respectively, based on $L1_2$ crystal structure with 20 Å of vacuum (to reduce self-interaction), was optimized using PBE functional [48] with 16x16x1 k-point grid and 400 eV plane wave cutoff energy until forces on all individual atoms were less than 0.08 eV/Å.

To study charge transfer, Bader charge analysis was performed using an algorithm described in the work by Tang et al [49] and VMD[50] was used for visualization of the results.

3. Results and discussion

3.1. Optical and morphological properties

Optical measurements (UV/Vis spectroscopy and spectroscopic ellipsometry) taken one day after the sample fabrication (Figure 1) show that the treatment enables broad tuning of the LSPR starting from blue (approx. 450 nm), through the entire visible spectrum, and ending in the near infrared (approx. 950 nm). Although the LSPR is undoubtedly affected by the Au deposition on the nanoparticle surface, which shifts the LSPR to red, the degree of tuning exceeds the range achievable purely by composition change

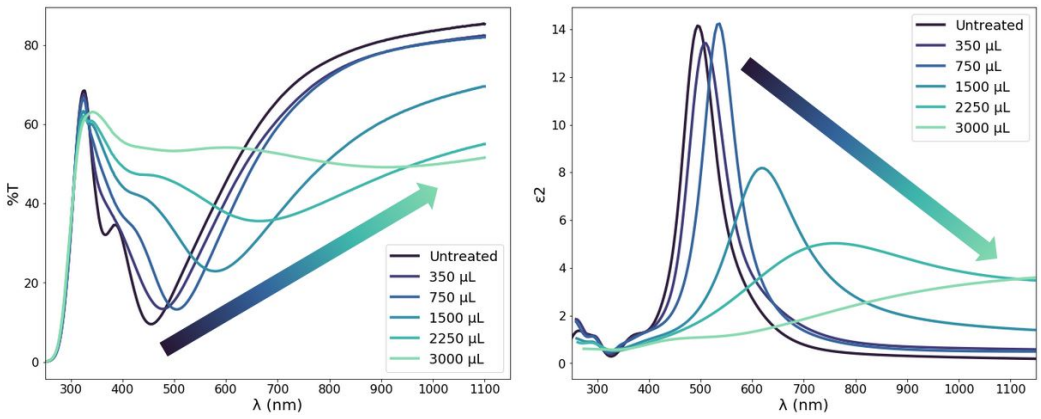

Figure 1: Left: Initial transmittance spectra for samples ranging from untreated to treated with 3000 μL of 2 mM $HAuCl_4$. The arrow depicts the trend of minima shift, which relates to the shift of plasmon resonance. Right: Initial imaginary part of the dielectric function for aforementioned samples. The arrow depicts the trend of maxima shift, which relates to the shift of plasmon resonance.

Sample	Pure Ag	350 μL	750 μL	1500 μL	2250 μL	3000 μL
λ_{LSPR} (nm)	455	477	505	580	663	911

Table 1: Plasmon peak position (λ_{LSPR}) as determined from the wavelength at transmittance minimum for the investigated samples

from Ag to Au. Large tunability indicates that morphological changes are likely responsible for the full magnitude of the LSPR shift. The initial trend is a smooth and slightly nonlinear red shift of the plasmon resonance with the increase of the total treatment agent ($HAuCl_4$) volume. Simultaneously with the red shift, both the transmittance minima and the peaks of the imaginary part of the dielectric function (ε_2) get broader and less prominent. Less light absorbed and/or scattered indicates that plasmon quenching is taking place as treatment progresses.

SEM pictures reveal systematic morphological changes with treatment progression of nanoislands, both at the individual and the group level. Individually, nanoislands change shape from quasi-hemispherical when untreated to polyhedral and irregular with sharper edges, after which one or more pinholes are gradually formed and expanded, finally forming a ring or a cage-like structure. There is also a trend of individual nanoislands merging into progressively larger nanostructures, resulting in about a micrometer-

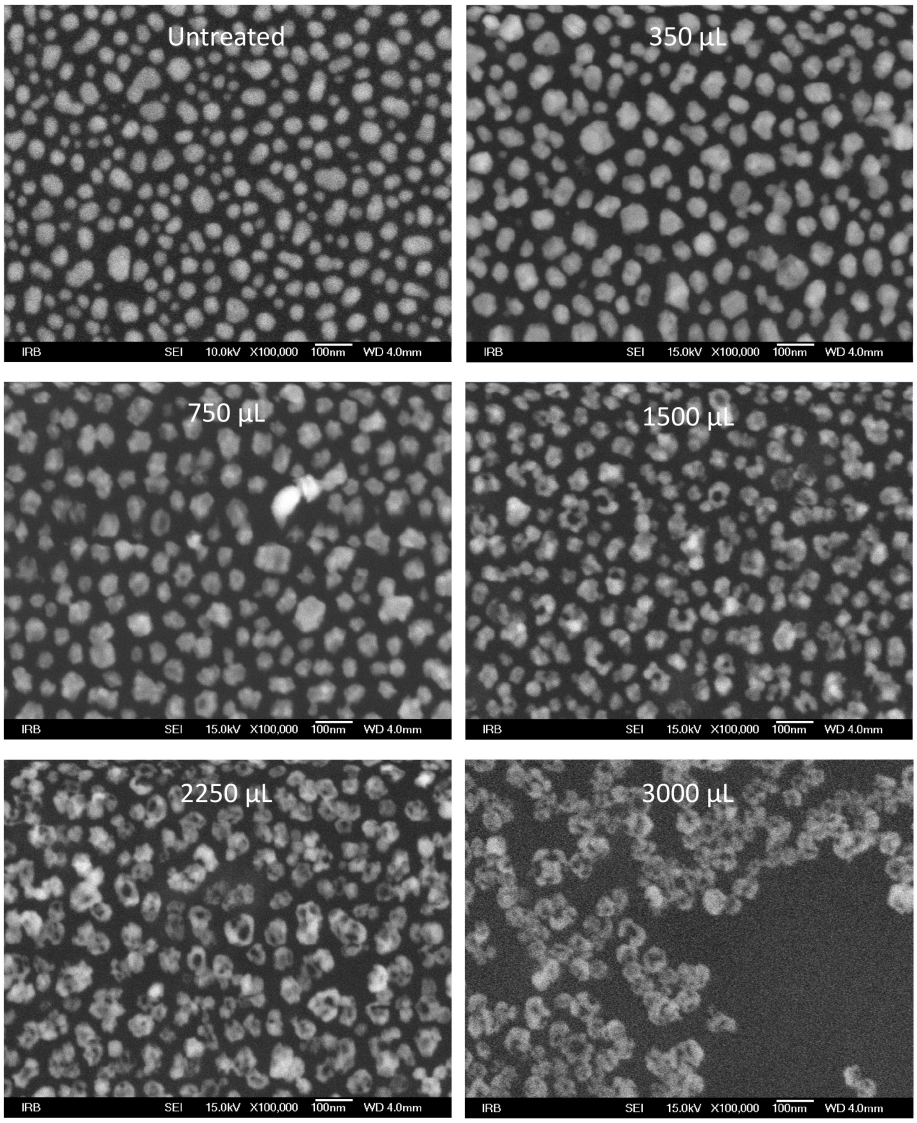

Figure 2: Scanning electron microscopy images for the for the samples ranging from untreated to treated with 3000 μL of 2 mM $HAuCl_4$. All micrographs are taken at the same magnification

long agglomerated formations resembling microchains of nanorings (Figure 2). Nanoparticle size distributions become wider with more treatment (Figure S13). It is also visible that interparticle distances range between almost zero, to about 20 nm, but become much larger for the μL sample due to

agglomeration and possible material loss. We note that SEM pictures were taken for aged samples, so possible morphological changes with ageing are also present.

All of the aforementioned morphological changes - the appearance of sharper edges, [51] hollowing, [52, 53] and agglomeration [54, 55] - could be contributing to the red shift. Moreover, the shift magnitude indicates that the morphological effects dominate for highly treated samples. Consistent with the SEM pictures, the features of the dielectric function (Figure 1 and Figure S2) also testify to the near-percolation behavior for the highly treated (2250 and 3000 μL) samples, as the nanoislands become interconnected. The ε_2 plateau at higher wavelengths, exhibited by the sample treated with 3000 μL of 2mM $HAuCl_4$, is typical for near-percolated nanostructures. [15, 56]

The pinhole formation is a standard consequence of the galvanic replacement reaction.[57] During galvanic replacement, the nanoislands of a less noble metal (lower reduction potential, in this work Ag) are used as a sacrificial template which reduces the cations of a more noble metal (higher reduction potential, in this work Au). During the reaction Au is being deposited on the surface of Ag nanoislands. The initial deposition forms a thin layer that can consist of pure Au [58, 59] or Au-Ag alloy [57, 60]. Reaction progression thins out the sacrificial metal, multiplies and expands the pinholes, which leads to the formation of nanoframes and nanorings as shown in the Figure 2. The resulting nanostructures are formed homogeneously over the whole sample surface that contained the initial silver nanoislands. This shows that our method, consisting of Ag deposition and annealing with subsequent galvanic replacement procedure using $HAuCl_4$, serves as a simple and large-area nanofabrication procedure that allows great tunability of optical and plasmonic properties. As such, it is suitable for high-throughput fabrication for many types of plasmon-based devices.

3.2. Stability investigation

Another necessary property for practical application of such devices is stability. We have achieved satisfactory mechanical stability (adhesion to the substrate) by optimizing the annealing procedure, as described in the Methods section and shown in the Figure S1. Two other important facets of stability are chemical resistance and preservation of morphology. For this reason, we have conducted subsequent optical measurements a few days, and also five months after the first ones. The observed changes provided us with the aging profile of the samples and enabled us to asses their overall stability.

During the ageing period the samples were stored in a (non-hermetically) closed transparent plastic box and held at room temperature. As evident from the Figure 3, after 5 months the optical properties of the samples have changed dramatically. Samples treated with 350, 750 and 1500 μL of $HAuCl_4$ solution now have a similar LSPR position. Pure silver shifted to the red far enough that the trend of LSPR shift with treatment is broken - although untreated, it is now red shifted when compared to the all aforementioned samples. LSPR position of the 2250 sample has, however, remained relatively unchanged. The appearance of a shoulder with long ageing times in the NIR region, seen in the transmittance measurements for samples treated with up to 1500 μL of the reagent, can likely be attributed to continued gradual agglomeration. In the Figure 2 agglomerates can be observed on the SEM pictures that were done on the aged samples. As nanoislands agglomerate the resulting Au-Ag hybrid metal nanoisland should shift the LSPR to the NIR region. Ellipsometry measurements are consistent with that assumption, as ε_2 curves also form a shoulder in the NIR, and are continuously increased at higher wavelengths with respect to the newly treated samples (Figure 1 and Figure 3). Finally, electrodynamics simulations of clustering effects also corroborate this assumption. As can be seen from Figure 3, a randomly generated cluster in which a minimum gap between particles (20 nm) is assumed displays electromagnetic response with a well-defined plasmon resonance. When the minimum gap between particles is reduced, clustering occurs and a red-shifted shoulder progressively develops in the extinction spectra. It is attributed to coupled resonances of closely located particles excited by light polarized along the axis joining the particles, as shown in the near field simulations of the cluster (Figure S3).

The ageing profiles for each individual sample in the Figure 4 display the peculiarity of their ageing process. The trend for silver is largely as expected. It is known from literature that silver, when exposed to the atmospheric conditions, oxidizes forming a dielectric layer usually consisting of silver sulphide.[61] The red shift is caused by the increase in the dielectric constant at the interface with the Ag nanoparticle (dielectric overlayer vs air). It is important to note that the red shift after the first few days is significant, comparable to the further shift observed after 5 months (Figure 4).

The sample treated with 350 μL of reagent barely changes position after the initial treatment, and also during the first few days. Even after 5 months it shifts only a little, but contrary to the pure silver, it is a blue shift. The

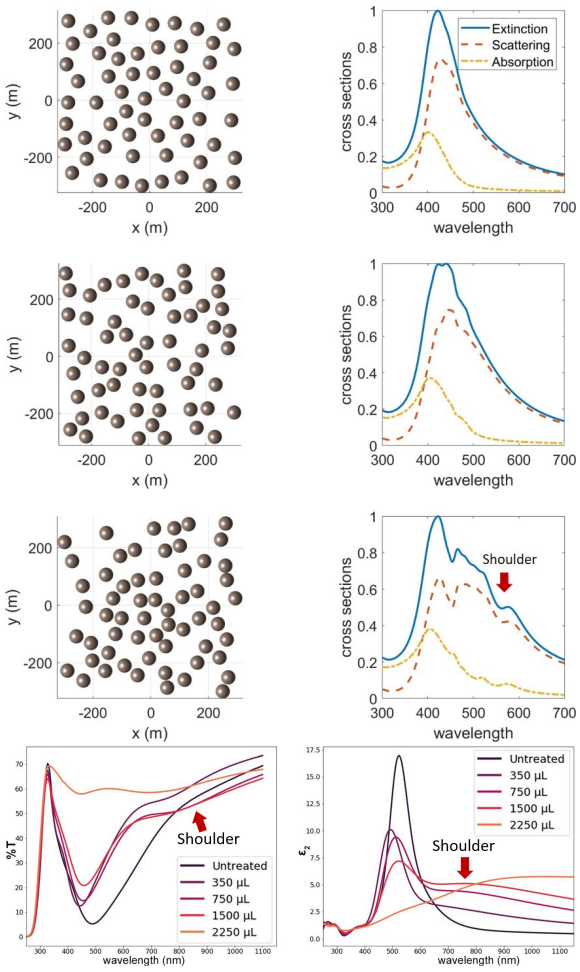

Figure 3: Top: Clusters of 60 $Ag_{0.85}Au_{0.15}$ particles (left) and corresponding electrodynamics response (right). Particles have a radius of 25 nm and are randomly located at the plane $z = 0$ allowing for a minimum interparticle distance of 20 (top), 10 (middle) and 0 nm (bottom). Cross sections are calculated in the framework of the multiple particle Mie theory assuming plane waves propagating in the z direction and averaged for x and y polarization. Refractive index of the embedding medium is 1.25, i.e. glass-air average. Bottom: Transmittance spectra for 5 months old samples ranging from untreated to treated with 3000 μL of 2 mM $HAuCl_4$ (left). Imaginary part of the dielectric function for 5 months old samples ranging from untreated to treated with 3000 μL of 2 mM $HAuCl_4$ (right).

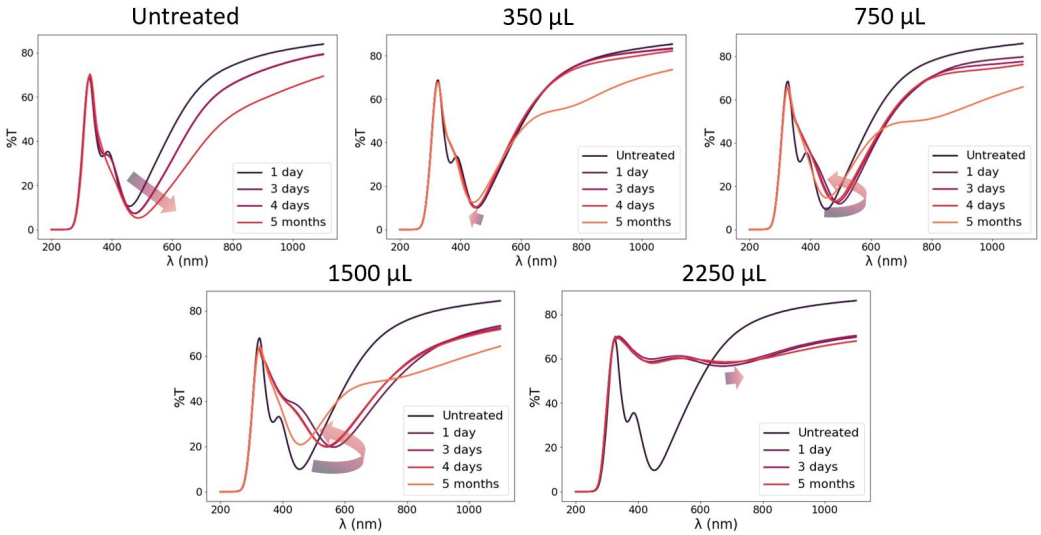

Figure 4: Trends of transmittance spectra changes for individual samples. Spectra show initial change with treatment, and subsequent changes with ageing at different times during 5 months. Arrows depict trends of transmission minima changes which follow the plasmon resonance shift.

750 μL sample, however, shows a clear trend reversal. After a prominent red shift due to the galvanic replacement, the transmittance minimum immediately starts shifting to blue and ends up almost at the same position as it had before it was treated. A similar but even more pronounced trend is present for the 1500 μL sample. However, another distinct trend can be observed for the 2250 μL sample. After a large red shift and an increase in the transmittance resulting from the sample treatment, there is very little further change with ageing. Transmittance minima for all samples, reflecting the plasmon position shift with treatment and ageing, is given in the Table S2.

To elucidate the reasons for different ageing trends and obtain more structural and compositional insights, TEM measurements were performed, and combined with electrodynamics simulations. 350 and 2250 μL samples were chosen for closer inspection since they are the most stable and thus the most promising ones. Moreover, they are the edge cases between which the trend reversal takes place, thus providing helpful insight to elucidate the types of changes happening in the other samples.

STEM-EELS analysis of the two samples shows two markedly different

morphologies and element distributions (Figure 5). The 350 μL sample is fully alloyed throughout the whole volume (additional EELS measurements showing individual particles are presented in Figure S15). There is no Au shell surrounding the nanoisland - on the contrary, there is rather little Au in the surface alloy composition. We propose that the slight blue shift that is observed can be attributed to morphological changes related to surface energy minimization (discussed later in the text), which could also explain the much larger blue shift with ageing that can be seen for 750 and 1500 μL samples. However, it is still unclear why there is a blue shift with respect to the initial pure silver for the 350 μL sample, as alloying even a small amount of gold should result in a small relative red shift. We believe that the reason could be in dielectric overlayer already forming on the Ag nanoisland surface before the initial optical measurements on the untreated sample, and slightly red shifting the plasmon resonance. As can be seen from the trends in Figure 4, there is already a notable shift in the first couple of days. Since the first measurement was performed 1 day after fabrication, some dielectric layer could have already formed and produced a noticeable red shift with regards to the LSPR of pristine silver. We hypothesize that the treatment with the small amount of reagent might lead to the removal of patina (dielectric overlayer), reversing the red shift. Simultaneously, a very small amount of gold deposited on the surface would shift the plasmon peak back near the starting point.

To test, and further clarify this hypothesis, an aged silver sample was subjected to the experimental procedure based on the one designed for galvanic replacement (described in the Methods section) but modified - without using the galvanic replacement reagent, $HAuCl_4$ - just pure milli Q water (MQW, 18 MΩ cm^{-1}), and rinsing with pure ethanol. Measurements taken immediately afterwards show a blue shift even when compared to silver nanoislands aged for only 1 day (Figure S7). Combined with the electrodynamics simulations (Figure S4) which also show that LSPR of pure silver nanoparticles is blue shifted in comparison to silver with a thin Ag_2S overlayer (the most likely corrosion product) [61], the results imply the removal of the dielectric overlayer during such treatment, even without galvanic replacement.

In contrast to the 350 μL sample, while there is some alloying on the nanoisland imaged by STEM-EELS on the aged 2250 μL sample, the elements are mostly separated. Element separation can occur due to dealloying in the later stages of the galvanic replacement process, when Ag atoms are being removed from the surface of the nanoparticle, leaving only Au. [62] The

irregular Ag island, with pinholes formed due to galvanic replacement process, is in part covered by Au shell-like structure. However, it is interesting to note that Au seems to have gathered in the pinholes, partially filling them. The preferential pinhole filling by deposited Au could be directed by surface energy minimization, leading to (incomplete) restoration of hemisphericity. A similar effect was observed in the work by Chien et al, [63] where solid nanoparticles were formed by Au preferentially backfilling the central void in the Au-Ag hollow nanoparticles formed by galvanic replacement. Au is also seen accumulating at the nanoisland edges, possibly contributing to nanoisland agglomeration and merging that was observed with larger treatment volumes.

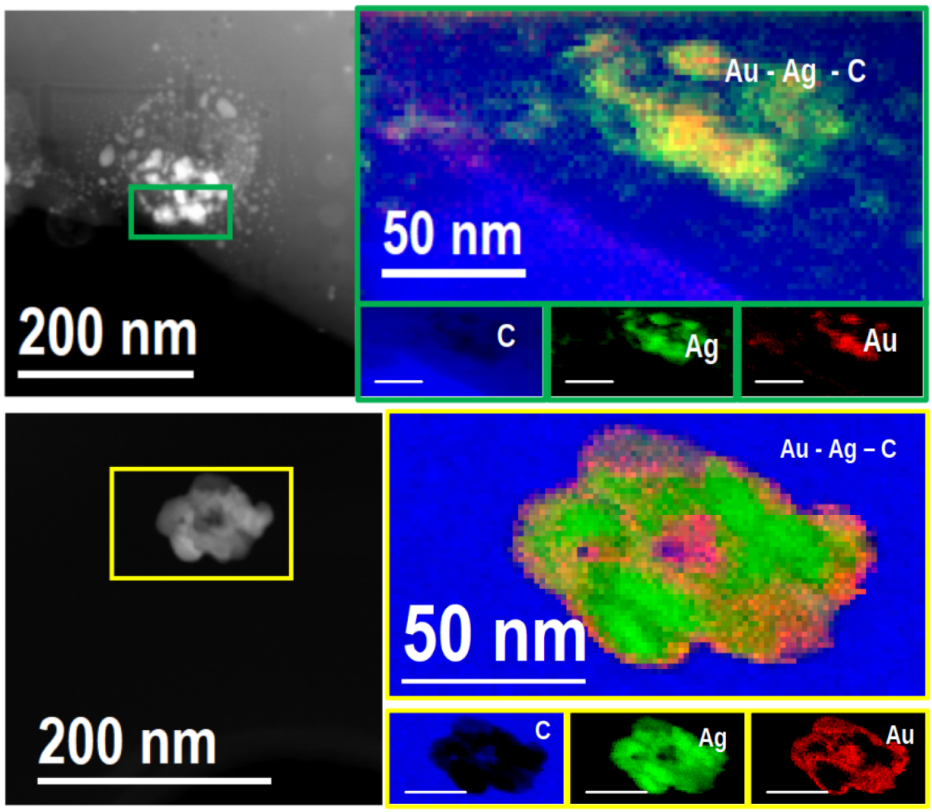

Figure 5: STEM-EELS map of the 350 μL sample (top) and 2250 μL sample (bottom). Near-complete overlap in the distribution maps of Ag and Au implies that the 350 μL sample is fully alloyed, while the distribution maps of the 2250 μL sample illustrate a more segregated, core-shell-like structure.

Unlike the samples treated with 350 μL and 2250 μL of $HAuCl_4$, those treated with 750 μL and 1500 μL showed considerable changes in the transmittance spectra with ageing. As possible explanations, we discuss compositional restructuring by Au-Ag interdiffusion, and purely morphological restructuring.

Since the strong blue shift is present for the samples which are treated more than the 350 μL sample, but less than the 2250 μL sample, we hypothesized that after the treatment they might possess a Au shell responsible for the initial red shift, which dissappears with time due to slow element interdiffusion at room temperature. There are several condition that could enable the spontaneus low-temperature alloying, such as large number of vacancies formed by galvanic replacement (playing an important role in Kirkendall effect), large interface area between core and shell elements enabling short-circuit diffusion paths, a substantial defect density in nanoislands, and the presence of stress-fields and dislocations. [64, 58, 65, 66] However, our electrodynamics simulations (Figure S5) show that transition from core-shell to alloyed structure could lead to blue shift only when Au shell would make up about 50% or more of the total nanoisland composition. In fact, the shift would be in the opposite direction with the atomic ratio of Au lower than 50%. Since such large Au ratio is not observed (EDS analysis showed up to 20% of Au in the nanoislands), the compositional restructuring can likely be discarded as a cause for the blue shift.

Morphological restructuring that leads to the LSPR blue shift is likely driven by surface energy minimization. Treated nanoparticles take an irregular shape with sharper edges, and form pinholes. Both of these characteristics can, as previously stated, lead to red shift, but also increase the surface energy. Surface energy minimization by respherification could partially reverse each process, while simultaneously shifting the LSPR back to the blue. Respherification has been determined as the reason for the observed blue shift with ageing after galvanic replacement by Yang et al [67]. Reduction of the pinhole has also been reported by Sun et al [62] and attributed to mass diffusion, while STEM-EELS pictures of 2250 μL sample in Figure 5 show Au preferentially filling the pinholes in Ag nanoisland, suggesting such filling is a possibility in the less treated samples too. Furthermore, computational studies of Au-Ag alloyed and core-shell particles with a pinhole, have demonstrated that hole reduction leads to substantial blue shift[68, 69] We thus believe that gradual respherification, likely involving partial hole reduction or filling, leads to the observed blue shift of LSPR with ageing.

The simultaneous appearance of the shoulder around 800 nm can, as shown by simulations in Figure 3, be attributed to the effect of partial agglomeration. Agglomeration is not very prominent for 350 μL sample, attesting to its morphological stability. However, it is more evident for 750 μL and 1500 μL samples (Figure 2, SEM pictures).

In light of these findings, we stress the importance of ageing measurements when assessing the potential of a system involving similar multimetallic nanostructures. As shown here, the initial properties might be short-lived even in mild conditions, which limits the applicability of the results reported without stability assessment.

With regards to the sample stability, it is important to note that the transmittance minimum of the 350 μL sample did not red shift, although there is no gold shell protecting it from the atmosphere and preventing the growth of a dielectric layer which happens on pure Ag sample. Since its surface consists primarily of Ag, the lack of red shift due to Ag reacting with air suggests that alloying with a small amount of Au is sufficient to passivize the surface and increase the long-term chemical stability of the nanoisland. Indeed, it has been widely reported that alloying greatly increases the chemical stability of the nanoparticles. [16, 17, 70, 71, 72, 73, 74, 75] Transmittance minima of the 750 μL and 1500 μL samples also ended up close to the minima of the untreated samples after 5 months of ageing. The final positions show a very small progressive red shift as the volume of the $HAuCl_4$ increases which poin ts to passivization of nanoislands, regardless of alloyed or core-shell structure. The samples treated with up to 1500 μL have a transmission minima at slightly higher wavelengths following the increase in the volume of the reagent (consistent with composition change), but the differences in LSPR are still much lower than the final shift caused by dielectric overlayer enveloping the surface of the nanoisland. Furthermore, instead of decreasing, as was observed with ageing of untreated Ag nanoislands, the transmittance is very slightly increasing with ageing.

It is clear that adding an Au shell passivizes the Ag core because the Ag atoms can't get in contact with the atmospheric molecules. Interestingly, alloying Au and Ag also leads to substantial passivization although surface Ag atoms aren't protected. The increased stability of Au-Ag alloyed nanostructures in comparison with pure Ag nanostructures has been found under various conditions and in different environments. Stability is increased in aqueous solutions [16, 17] even in the presence of leeching electrolytes[71, 72]. Alloyed nanostructures have also shown chemical stability in oxidative mix-

tures known to dissolve pure Ag [73], even after 12 hours of exposure [74]. Finally, in air, Ag-Au nanoalloys have shown long-term ageing resistance (during 3 months) [75] and combined chemical and thermal stability during calcination (10 minutes at 600 ℃ [74] and 300 ℃ for 12 hours). [70]. However, the exact reasons for the stability increase upon Au addition are still unclear. Entropic effects, Ag depletion (leading to Au shell formation), difficulty of oxygen diffusibility, silver-oxygen bonding, effects due to alloy structure, and charge-transfer effects have been mentioned as possible reasons. [16, 71]

Here, we focused on the charge-transfer effects, as they should be present always, regardless of the environment or the conditions. By using density functional theory (DFT) we explored the charge distribution on a model alloy system, a semi-infinite thin film of Ag-Au alloy with a respective 3 to 1 ratio (Figure S6). Charge analysis shows that electron density has partially moved from Ag to Au (Table S1). Au atoms in such a system are significantly negatively charged, drawing approximately 0.3 electrons in total from the surrounding Ag atoms. Consequently, Ag atoms carry a partial positive charge, losing approximately 0.1 electron. Inducing a partial positive charge on Ag atoms makes them less prone to electron donation (oxidation) and thus less reactive with oxidative species in the environment. Charge-transfer effects thus explain, at least in part, the higher chemical resistance of Au-Ag nanoalloys, in comparison with pure Ag nanostructures.

3.3. Surface-enhanced Raman scattering (SERS) study

Rough gold and silver surfaces have been widely used as substrates for Raman scattering enhancement, allowing detection and structural analysis of molecules at low concentrations. [76] To study the SERS efficiency of the prepared metallic nanostructures, 4-aminothiophenol (4-ATP) and rhodamine 6G (R6G) were used. Owing to high scattering ability and substituent driven adsorption, these aromatic compounds have been commonly used as model molecules in the SERS spectroscopy. [77, 78] Assignment of the bands is presented in the Supporting information, "Assignment of Raman bands" section. The Raman bands of model molecules were excited using laser at two wavelengths, 532 nm (results shown in Figures S10 and S11 of Supporting information) and 785 nm (results shown here).

The SERS spectra of 4-ATP ($c = 1 \times 10^{-5}$ M) on the prepared aged metallic substrates were obtained and compared to the Raman spectrum of solid 4-ATP (Figure 6). Interestingly, the SERS spectra of 4-ATP clearly differed

from the Raman spectrum of the solid sample. New, intense bands were assigned to NN stretching mixed with CH deformation (1430 and 1390 cm^{-1}) as well as to C-N stretching (1140 cm^{-1}). [79] Appearance of these bands in the SERS spectra of 4-ATP pointed to existence of new species on the metallic substrates. It was assumed that dimers of 4-ATP molecules were formed (4,4-dimercaptoazobenzene, DMAB), by linking two monomeric molecules through amino groups. This was in agreement with the findings that laser light can induce dimerization of 4-ATP molecules on rough silver surface. [79, 35]

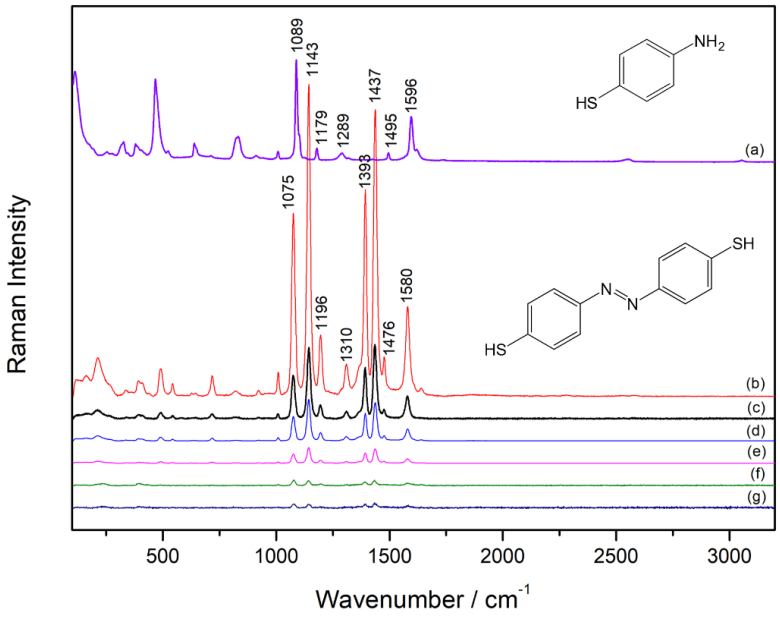

Figure 6: Raman spectrum of solid 4-ATP (a) and SERS spectra of 4-ATP, c = 1×10^{-5} M, on: Ag + Au (350) (b), pure Ag (c), Ag + Au (750) (d), Ag + Au (1500) (e), Ag + Au (2250) (f), Ag + Au (3000) (g); laser wavelength: 785 nm, laser power: 16 mW (a) and 0.1 mW (b-g). The spectra are displaced for visual clarity.

Among all the tested metallic substrates, the strongest enhancement of the Raman scattering was obtained for 4-ATP on the fully alloyed Au-Ag nanostructure (Ag treated with 350 μL $HAuCl_4$), characterized by increased stability but preserved plasmonic properties of silver. By further increase in gold content, the intensity of the SERS spectra diminished, being the weakest for 4-ATP molecules adsorbed on the nanoislands with the highest Au content (Ag treated with 3000 μL $HAuCl_4$). Although SERS efficiency

of pure Ag nanoislands is considerably lower than that of the 350 μL sample, it surpassed the enhancing ability of the rest of the treated samples.

Apart from the difference in the overall SERS intensity, relative intensity of the spectral bands changed with the metal composition of the tested substrates. Hence, the intensity ratio of the C-S stretching band (1075 cm^{-1}) and C-N stretching band (1143 cm^{-1}) varied from 0.610 (Ag) to 1.095 (Ag treated 3000 μL of $HAuCl_4$), indicating nanostructure dependent orientation of DMAB molecules towards the metallic surface. Due to high affinity of nitrogen atoms for silver surface, the molecules were most likely placed on the silver-based nanostructures with the central azo moiety close to the surface, whereas adsorption of the molecules through sulfur atom was very likely favored on the nanostructures constituting mostly of gold.

The SERS spectra of R6G (c = 1×10^{-5} M) on different metallic nanostructures followed the same trend as the spectra of 4-ATP. The Raman scattering, as shown on Figure 7, was enhanced at most for R6G molecules adsorbed on the treated metallic substrate containing the least amount of Au (the 350 μL sample. By increasing the gold content, the SERS intensity decreased, though not as pronounced as in case of 4-ATP (DMAB). In addition, the composition of the metallic nanostructures did not affect the relative band intensity, leading to a conclusion that, regardless of the substrate used, the preferred orientation of R6G molecules on the metal surface remained the same.

It should be emphasized that the SERS spectra of 4-ATP and R6G were taken using the laser power of 0.1 and 0.2 mW, respectively, three orders of magnitude lower than the maximum power, indicating excellent SERS efficiency of all the prepared metallic substrates, especially of the sample treated with 350 μL $HAuCl_4$.

It is visible from the trends in the Figures 6, 7, and S10 the 350 μL sample shows the best SERS performance regardless of the model molecule or the laser wavelength.

To verify the stability of the best performing sample we also performed measurements on a freshly prepared 350 μL sample, and additionally of freshly prepared 750 μL sample for comparison. The efficiencies of the aged and freshly prepared 350 μL samples are very similar, evidencing the stability of nanostructures prepared in such conditions (Figures S19-S21). Additionally, the relative SERS efficiencies of the freshly prepared 350 μL and 750 μL samples (Figures S16-S19) are consistent with those of the aged samples shown in Figure 6.

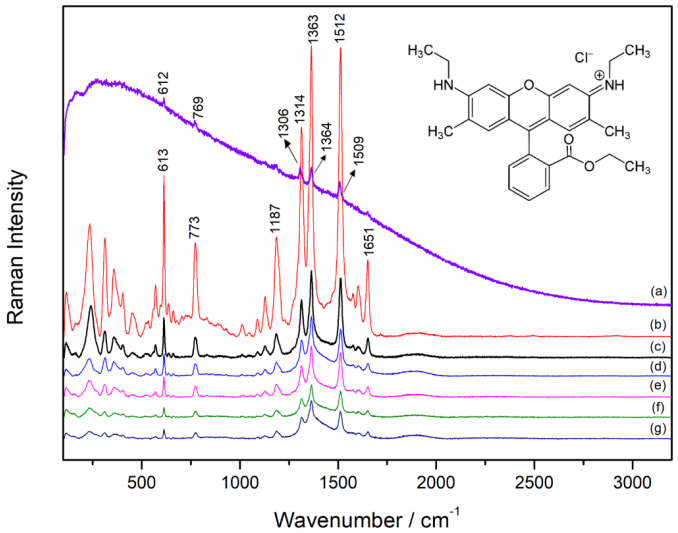

Figure 7: Raman spectrum of solid R6G (a) and SERS spectra of R6G, c = 1×10^{-5} M, on: Ag + Au (350) (b), pure Ag (c), Ag + Au (750) (d), Ag + Au (1500) (e), Ag + Au (2250) (f), Ag + Au (3000) (g); laser wavelength: 785 nm, laser power: 0.0003 mW (a) and 0.2 mW (b-g). The spectra are displaced for visual clarity.

While it seems intuitive to assume that SERS performance follows the LSPR intensity at the given wavelength, the relationship between these two phenomena is quite complicated. Indeed, for a long time, SERS based on the plasmonic properties was achieved without correlation with LSPR [14], although recent research is showing some progress in elucidating the relationship between SERS and LSPR [80].

In this context, although the main reason for the best SERS performance of the 350 μL sample with alloyed Au-Ag nanoislands might be difficult to asses, we suggest here some of the possible explanations:

(i) Based on the argumentation above, we believe that nanoislands in this sample do not form a patina (dielectric overlayer) as the pure Ag ones on the untreated sample. It has been reported that even a couple of nanometers thick dielectric layer dividing the model molecules from the surface of the nanoparticle can significantly reduce the SERS signal. [81] Our electrodynamics simulations are in agreement with the reported data, and show that even 1 nm thick Ag_2S shell covering Ag nanoparticle with a 25 nm radius results in a 4-fold reduction of the maximum near field enhancement. (ii) As a low amount of Au is added to the Ag nanoislands, the alloyed structure

shows superior field enhancement when compared to the core-shell structure (Figure S5), for certain compositions even comparable to pure silver [82]. (iii) Nanoislands in that sample can enhance the SERS performance because their sharp edges (Figure 2) can lead to more intense hot-spots [83, 84]. (iv) Islands on that sample have a relatively small interparticle distance (favorable for hot-spot intensity). However, in contrast to the more treated samples, very few of them merge (even after five months), and thus avoid reduction of the hot-spot number and intensity. [85]

Low agglomeration during a prolonged period with no special storage conditions makes this sample especially suitable for utilization in SERS and other sensing techniques. In fact, although in some of the more treated samples the nanoislands show more agglomeration that likely increases with ageing, even they are still exceptionally stable when compared to the sensors based on nanoparticle aggregates. Such aggregates lack stability and suffer from low reproducibility. [9] Due to the aforementioned reasons, aggregates are severely limited for practical applications regardless of the performance, which points to nanoislands as a promising alternative.

Detection limit measurements for 4-ATP and R6G on the most SERS-efficient sample (treated with 350 μL of reagent) are shown in the Figures S8 and S9. Details regarding the procedure are presented in the Supplementary information, "Detection limit measurements" section.

Detection was possible in the nanomolar range (1×10^{-7} M) displaying the high detectability of the substrate. Such detection limit is comparable to several different recently reported bimetallic Au-Ag nanostructures which also enable detection in the nanomolar range [86, 87, 88, 89, 90]. While some bimetallic structures enable detection even below the nanomolar range [91, 92] we note that our measurements were performed using very low laser power ($\leq$ 0.2 mW, approximately 1000 times lower than the maximum power). The SERS performance of our samples suggests that they might be especially suitable for measurements of the laser radiation sensitive samples such as cells and tissues since high detectability in mild conditions enables avoiding photoinduced destruction of the sample. Special methods have been developed to provide detectability under nondestructive conditions (reduced laser power), such as optical fibers with nanoislands at the tips [93, 94], and a recent study using a fiber-optrode with silver-coated gold nanostars reported the same limit of detection as in our work [95]. However, we believe that using bimetallic nanoislands on simple glass substrates, as shown in this work, is advantageous due to comparatively low cost, ease of production and much

better suitability for large-area nanofabrication.

The ability to modulate the morphology of nanoislands can also play a beneficial role for sensing capabilities due to multiple pinhole formation which induces nanoporosity. The resulting increase of surface area can enable adsorption of a larger amount of labeling agents. These molecules can then be used in SERS tags to detect the desired species by conjugating with them. Furhermore, hollow nanoislands have previously shown good performance for refractive index sensing, [40, 96] so the combination of stability and hollow morphology of the nanoislands produced by treatment with 2250 μL of reagent holds the prospect for said utilization.

4. Conclusion

In this work, we have demonstrated a large-area, simple, and inexpensive nanofabrication procedure for hybrid metal Au-Ag islands on glass substrates. Our procedure provides exceptional tunability, as morphology of the nanostructures can be tailored from fully alloyed to core-shell, and from individual hemispherical nanoislands to microchains of nanorings. Consequently, plasmon resonance can be tuned through the entire visible range, and well into the near infrared region.

Ageing measurements highlighted the critical importance of stability assessment in determining the practical applicability of plasmonic multimetal nanostructures, as morphology changes can continue for days, or even months after fabrication. DFT calculations demonstrated that charge transfer from Ag to Au helps explain the pronounced increase in chemical stability of Ag-based nanostructures as Au is added by alloying - an effect that is widely reported but not yet fully understood. Based on that, we identified fabrication conditions that lead to multifaceted stability: chemical resistance, mechanical stability (adhesion to the substrate), and morphological stability.

In SERS measurements, Au-Ag nanostructures enabled detectability limit in the nanomolar range even with very low laser power, which is especially suitable for use with sensitive biomaterials. Combined with tunability of plasmon resonance to wavelengths in the tissue transparency window, our samples show promise for use for SERS and LSPR-based sensing in biomedicine. Furthermore, glass substrates with thin nanoisland films, as produced with our method, should be easily integrable with microfluidics elements to form a lab-on-a-chip device, with potential use in next generation diagnostics.

Finally, we emphasize that Au-Ag alloyed nanostructures with the best SERS performance also remained almost unchanged with ageing, with plasmonic properties rivaling those of pure Ag nanoislands. Such a combination is universally useful and highly sought of in the field of plasmonics. Fabrication method for nanostructures with gold-like stability and silver-like plasmonic properties thus holds importance not only for sensing, but photocatalysis, solar energy harvesting, and other utilizations of plasmon-based properties.

Acknowledgements

The authors thank the financial support of the Croatian Science Foundation through the grant number IP-2019-04-5424. ICN2 acknowledges funding from Generalitat de Catalunya 2017 SGR 327. This study was supported by MCIN with funding from European Union NextGenerationEU (PRTR-C17.I1) and Generalitat de Catalunya. The authors thank support from "ERDF A way of making Europe", by the "European Union". ICN2 is supported by the Severo Ochoa program from Spanish MINECO (Grant No. SEV-2017-0706) and is funded by the CERCA Programme / Generalitat de Catalunya. MCS has received funding from the post doctoral fellowship Juan de la Cierva Incorporation from MICINN (JCI-2019) and the Severo Ochoa programme.

References

[1] A. R. Rastinehad, H. Anastos, E. Wajswol, J. S. Winoker, J. P. Sfakianos, S. K. Doppalapudi, M. R. Carrick, C. J. Knauer, B. Taouli, S. C. Lewis, A. K. Tewari, J. A. Schwartz, S. E. Canfield, A. K. George, J. L. West, N. J. Halas, Gold nanoshell-localized photothermal ablation of prostate tumors in a clinical pilot device study, PNAS 116 (2019) 18590–18596. doi:10.1073/pnas.1906929116.

[2] X. Geng, M. Abdellah, R. B. Vadell, M. Folkenant, T. Edvinsson, J. Sá, Direct plasmonic solar cell efficiency dependence on spiro-ometad li-tfsi content, Nanomaterials 11 (2021) 3329. doi:10.3390/nano11123329.

[3] InnoEnergy, Accelerating sustainable energy innovations.
URL `https://issuu.com/innoenergy/docs/product_catalogue_20_b2`

[4] M. McCoy, Using photocatalysis to make chemical reactions more efficient, C&EN 97 (2019) 46–47. doi:10.1021/cen-09744-cover10.

[5] Commercializing plasmonics, Nature Photonics 9 (2015) 477. doi:10.1038/nphoton.2015.149.

[6] P. Moitra, M. Alafeef, K. Dighe, M. B. Frieman, D. Pan, Selective Naked-Eye Detection of SARS-CoV-2 Mediated by N Gene Targeted Antisense Oligonucleotide Capped Plasmonic Nanoparticles, ACS Nano 14 (2020) 7617–7627. doi:10.1021/acsnano.0c03822.

[7] D. Quesada-González, M. A., Nanoparticle-based lateral flow biosensors, Biosensors & bioelectronics 73 (2015) 47–63. doi:10.1016/j.bios.2015.05.050.

[8] P. Estrela, K. M. Koczula, A. Gallotta, Lateral flow assays, Essays in Biochemistry 60 (2016) 111–120. doi:10.1042/EBC20150012.

[9] C. Caro, P. M. Castillo, R. Klippstein, D. Pozo, A. P. Zaderenko, Silver nanoparticles: Sensing and imaging applications, in: D. P. Perez (Ed.), Silver Nanoparticles, IntechOpen, Rijeka, 2010, Ch. 11. doi:10.5772/8513.
URL `https://doi.org/10.5772/8513`

[10] C. Levard, E. M. Hotze, G. V. Lowry, G. E. B. Jr., Environmental Transformations of Silver Nanoparticles: Impact on Stability and Toxicity, Environmental Science & Technology 46 (2012) 6900–6914. doi:10.1021/es2037405.

[11] M. Erol, Y. Han, S. K. Stanley, C. M. Stafford, H. Du, S. Sukhishvili, SERS Not To Be Taken for Granted in the Presence of Oxygen, Journal of the American Chemical Society 131 (2009) 7480–7481. doi:10.1021/ja807458x.

[12] M. J. Khan, S. Kumari, J. Selamat, K. Shameli, A. Q. Sazili, Reducing Meat Perishability through Pullulan Active Packaging, Journal of food quality 2020 (2020) 8880977. doi:10.1155/2020/8880977.

[13] M. Mayer, A. M. Steiner, D. F. Röder, D. P. Formanek, D. T. A. F. König, P. D. A. Fery, Aqueous Gold Overgrowth of Silver Nanoparticles: Merging the Plasmonic Properties of Silver with the Functionality

of Gold, Angewandte Chemie International Edition 56 (2017) 15866–15870. doi:10.1002/anie.201708398.

[14] T. Chung, Y. Lee, M.-S. Ahn, W. Lee, S.-I. Bae, C. S. H. Hwanga, K.-H. Jeong, Nanoislands as plasmonic materials, Nanoscale 11 (2019) 8651–8664. doi:10.1039/C8NR10539A.

[15] S. Badilescu, D. Raju, S. Bathini, M. Packirisamy, Gold Nano-Island Platforms for Localized Surface Plasmon Resonance Sensing: A Short Review, Molecules 25 (2020) 4661. doi:10.3390/molecules25204661.

[16] N. Alissawi, V. Zaporojtchenko, T. Strunskus, I. Kocabas, V. S. K. Chakravadhanula, L. Kienle, D. Garbe-Schönberg, F. Faupel, Effect of gold alloying on stability of silver nanoparticles and control of silver ion release from vapor-deposited Ag–Au/polytetrafluoroethylene nanocomposites, Gold Bulletin 46 (2013) 3–11. doi:10.1007/s13404-012-0073-6.

[17] S. Besner, M. Meunier, Femtosecond Laser Synthesis of AuAg Nanoalloys: Photoinduced Oxidation and Ions Release, Journal of Physical Chemistry C 114 (2010) 10403–10409. doi:10.1021/jp102461u.

[18] T. Gong, P. Lyu, K. J. Palm, S. Memarzadeh, J. N. Munday, M. S. Leite, Emergent opportunities with metallic alloys: from material design to optical devices, Advanced Optical Materials 8 (23) (2020) 2001082. doi:10.1002/adom.202001082.

[19] F. Zheng, W. K. an Lixia Shi, H. Liu, Y. Zhao, Plasmonic Au–Ag Janus Nanoparticle Engineered Ratiometric Surface-Enhanced Raman Scattering Aptasensor for Ochratoxin A Detection, Analytical Chemistry 91 (2019) 11812–11820. doi:10.1021/acsphotonics.8b01369.

[20] P. Nandhagopal, A. K. Pal, D. Bharathi Mohan, Fabrication of silver and silver-copper bimetal thin films using co-sputtering for SERS applications, Optical Materials 97 (2019) 109381. doi:10.1016/j.optmat.2019.109381.

[21] A. K. Pal, D. Bharathi Mohan, SERS enhancement, sensitivity and homogeneity studies on bi-metallic Ag-Cu films through tuning of broad band SPR towards red region, Journal of Alloys and Compounds 698 (2017) 460–468. doi:10.1016/j.jallcom.2016.12.246.

[22] J. Zhao, L. Jensen, J. Sung, S. Zou, G. C. Schatz, , R. P. V. Duyne, Interaction of Plasmon and Molecular Resonances for Rhodamine 6G Adsorbed on Silver Nanoparticles, Journal of American Chemical Society 126 (2007) 7647–7656. doi:10.1021/ja0707106.

[23] A. J. Haes, S. Zou, J. Zhao, G. C. Schatz, , R. P. V. Duyne, Localized Surface Plasmon Resonance Spectroscopy near Molecular Resonances, Journal of American Chemical Society 128 (2008) 10905–10914. doi:10.1021/ja063575q.

[24] A. Das, J. Zhao, G. C. Schatz, S. G. Sligar, R. P. V. Duyne, Screening of type i and ii drug binding to human cytochrome P450-3A4 in nanodiscs by localized surface plasmon resonance spectroscopy, Analytical Chemistry 81 (2009) 3754–3759. doi:10.1021/ac802612z.

[25] B. Ren, G.-K. Liu, X.-B. Lian, Z.-L. Yang, Z.-Q. Tian, Raman spectroscopy on transition metals, Analytical and Bioanalytical Chemistry 388 (2007) 29–45. doi:doi.org/10.1007/s00216-007-1141-2.

[26] Z.-Q. Tian, B. Ren, D.-Y. Wu, Surface-Enhanced Raman scattering: From Noble to Transition Metals and from Rough Surfaces to Ordered Nanostructures, Journal of Physical Chemistry B 106 (2002) 9463–9483. doi:10.1021/jp0257449.

[27] X. Wang, W. Shi, G. Shea, L. Mu, Surface-Enhanced Raman Scattering (SERS) on transition metal and semiconductor nanostructures, Physical Chemistry Chemical Physics 14 (2012) 5891–5901. doi:10.1039/C2CP40080D.

[28] W. Xu, N. Mao, J. Zhang, Graphene: A Platform for Surface-Enhanced Raman Spectroscopy, small 9 (2013) 1206–1224. doi:10.1002/smll.201203097.

[29] F. Benz, R. Chikkaraddy, A. Salmon, H. Ohadi, B. de Nijs, J. Mertens, C. Carnegie, R. W. Bowman, J. J. Baumberg, SERS of Individual Nanoparticles on a Mirror: Size Does Matter, but so Does Shape, Journal of Physical Chemistry Letters 7 (2016) 2264–2269. doi:10.1021/acs.jpclett.6b00986.

[30] V. Merk, J. Kneipp, K. Leosson, Gap Size Reduction and Increased Sers Enhancement in Lithographically Patterned Nanoparticle Arrays

by Templated Growth, Advanced Optical Materials 1 (2013) 313–318. doi:10.1002/adom.201200061.

[31] S. Kessentini, D. Barchiesi, C. D'Andrea, A. Toma, N. Guillot, E. D. Fabrizio, B. Fazio, O. M. Maragó, P. G. Gucciardi, M. L. de la Chapelle, Gold Dimer Nanoantenna with Slanted Gap for Tunable LSPR and Improved SERS, Journal of Physical Chemistry C 118 (2014) 3209–3219. doi:10.1021/jp409844y.

[32] H. Yockell-Lelièvre, F. Lussier, J.-F. Masson, Influence of the Particle Shape and Density of Self-Assembled Gold Nanoparticle Sensors on LSPR and SERS, Journal of Physical Chemistry C 119 (2015) 28577–28585. doi:10.1021/acs.jpcc.5b09570.

[33] Ángela I. López-Lorente, Recent developments on gold nanostructures for surface enhanced Raman spectroscopy: Particle shape, substrates and analytical applications. A review, Analytica Chimica Acta 1168 (2021) 338474. doi:10.1016/j.aca.2021.338474.

[34] K. Uetsuki, P. Verma, T.-A. Yano, Y. Saito, T. Ichimura, S. Kawata, Experimental identification of chemical effects in surface enhanced Raman scattering of 4-aminothiophenol, The Journal of Physical Chemistry C 114 (2010) 7515–7520. doi:10.1021/jp9114805.

[35] Y. Ke, B. Chen, M. Hu, N. Zhou, Z. Huang, G. Meng, In-situ monitoring the SERS spectra of para-aminothiophenol adsorbed on plasmon-tunable Au@Ag core-shell nanostars, Nanomaterials 12 (2022) 1156. doi:10.3390/nano12071156.

[36] S. E. J. Bell, G. Charron, E. Cortés, J. Kneipp, M. L. de la Chapelle, J. Langer, M. Procházka, V. Tran, S. Schlücker, Towards Reliable and Quantitative Surface-Enhanced Raman Scattering (SERS): From Key Parameters to Good Analytical Practice, Angewandte Chemie International Edition 59 (2019) 5454–5462. doi:10.1002/anie.201908154.

[37] G. Barbillon, Fabrication and SERS Performances of Metal/Si and Metal/Zno Nanosensors: A Review, Coatings 9 (2019) 7–25. doi:10.3390/coatings9020086.

[38] M. Fan, G. F. Andrade, A. G. Brolo, A review on the fabrication of substrates for surface enhanced Raman spectroscopy and their applications in analytical chemistry, Analytica Chimica Acta 693 (2011) 7–25. doi:10.1016/j.aca.2011.03.002.

[39] E. Hemmer, A. Benayas, F. Légaré, F. Vetrone, Exploiting the biological windows: current perspectives on fluorescent bioprobes emitting above 1000 nm, Nanoscale Horizons 1 (3) (2016) 168–184. doi:10.1039/C5NH00073D.

[40] I. Fabijanić, M. Mičetić, M. Bubaš, V. Janicki, S. Bernstorff, J. Sancho-Parramon, Hollow metal island films as plasmonic sensors produced by galvanic replacement, Surfaces and Interfaces 10 (2021) 101483. doi:10.1016/j.surfin.2021.101483.

[41] A. L. Aden, M. Kerker, Scattering of electromagnetic waves from two concentric spheres, Journal of Applied Physics 22 (10) (1951) 1242–1246. doi:10.1063/1.1699834.

[42] O. P. na Rodríguez, M. Caro, A. Rivera, J. Olivares, J. M. Perlado, A. Caro, Optical properties of au-ag alloys: An ellipsometric study, Opt. Mater. Express 4 (2) (2014) 403–410. doi:10.1364/OME.4.000403.

[43] J. Gérardy, M. Ausloos, Absorption spectrum of clusters of spheres from the general solution of maxwell's equations. ii. optical properties of aggregated metal spheres, Physical Review B 25 (6) (1982) 4204. doi:10.1103/PhysRevB.25.4204.

[44] J. J. Mortensen, L. B. Hansen, K. W. Jacobsen, Real-space grid implementation of the projector augmented wave method, Physical Review B 71 (2005) 035109. doi:10.1103/PhysRevB.71.035109.

[45] J. Enkovaara, C. Rostgaard, J. J. Mortensen, J. Chen, M. Dułak, L. Ferrighi, J. Gavnholt, C. Glinsvad, V. Haikola, H. A. Hansen, H. H. Kristoffersen, M. Kuisma, A. H. Larsen, L. Lehtovaara, M. Ljungberg, O. Lopez-Acevedo, P. G. Moses, J. Ojanen, T. Olsen, V. Petzold, N. A. Romero, J. Stausholm-Møller, M. Strange, G. A. Tritsaris, M. Vanin, M. Walter, B. Hammer, H. Häkkinen, G. K. H. Madsen, R. M. Nieminen, J. K. Nørskov, M. Puska, T. T. Rantala, J. Schiøtz, K. S. Thygesen,

K. W. Jacobsen, Electronic structure calculations with GPAW: a real-space implementation of the projector augmented-wave method, Journal of Physics: Condensed Matter 22 (25) (2010) 253202. doi:10.1088/0953-8984/22/25/253202.
URL https://doi.org/10.1088\%2F0953-8984\%2F22\%2F25\%2F253202

[46] A. H. Larsen, J. J. Mortensen, J. Blomqvist, I. E. Castelli, R. Christensen, M. Dułak, J. Friis, M. N. Groves, B. Hammer, C. Hargus, E. D. Hermes, P. C. Jennings, P. B. Jensen, J. Kermode, J. R. Kitchin, E. L. Kolsbjerg, J. Kubal, K. Kaasbjerg, S. Lysgaard, J. B. Maronsson, T. Maxson, T. Olsen, L. Pastewka, A. Peterson, C. Rostgaard, J. Schiøtz, O. Schütt, M. Strange, K. S. Thygesen, T. Vegge, L. Vilhelmsen, M. Walter, Z. Zeng, K. W. Jacobsen, The atomic simulation environment—a Python library for working with atoms, Journal of Physics: Condensed Matter 29 (27) (2017) 273002. doi:10.1088/1361-648X/aa680e.
URL http://stacks.iop.org/0953-8984/29/i=27/a=273002

[47] H. J. Monkhorst, J. D. Pack, Special points for Brillouin-zone integrations, Physical Review B 13 (2008) 5188. doi:10.1103/PhysRevB.13.5188.

[48] J. P. Perdew, K. Burke, M. Ernzerhof, Generalized gradient approximation made simple, Physical Review Letters 77 (1996) 3865–3868. doi:10.1103/PhysRevLett.77.3865.

[49] W. Tang, E. Sanville, G. Henkelman, A grid-based Bader analysis algorithm without lattice bias, Journal of Physics: Condensed Matter 21 (2009) 084204. doi:10.1088/0953-8984/21/8/084204.

[50] W. Humphrey, A. Dalke, K. Schulten, Vmd - visual molecular dynamics, Journal of Molecular Graphics and Modelling 14.1 (1996) 33–38. doi:10.1016/0263-7855(96)00018-5.

[51] W. Cao, T. Huang, X.-H. N. Xu, H. E. Elsayed-Ali, Localized surface plasmon resonance of single silver nanoparticles studied by dark-field optical microscopy and spectroscopy, Journal of Applied Physics 109 (2011) 034310. doi:10.1063/1.3544349.

[52] H.-P. Liang, L.-J. Wan, C.-L. Bai, L. Jiang, Gold Hollow Nanospheres: Tunable Surface Plasmon Resonance Controlled by Interior-Cavity Sizes, Journal of Physical Chemistry B 109 (2005) 7795–7800. doi:10.1021/jp045006f.

[53] A. Genç, J. Patarroyo, J. Sancho-Parramon, R. Arenal, M. Duchamp, E. E. Gonzalez, L. Henrard, N. G. Bastús, R. E. Dunin-Borkowski, V. F. Puntes, et al., Tuning the plasmonic response up: hollow cuboid metal nanostructures, ACS photonics 3 (5) (2016) 770–779. doi:10.1021/acsphotonics.5b00667.

[54] D. Chahinez, T. Reji, R. Andreas, Modeling of the surface plasmon resonance tunability of silver/gold core–shell nanostructures, RSC Advances 8 (2018) 19616. doi:10.1039/c8ra03261k.

[55] R. D. Babli Debnath, Presence of fluoride in water diminishes fast the spr peak of silver nanocrystals showing large red shift with quick sedimentation – a fast sensing and fast removal case, Spectrochimica Acta Part A: Molecular and Biomolecular Spectroscopy 249 (2021) 119306. doi:10.1016/j.saa.2020.119306.

[56] M. Bubaš, V. Janicki, S. A. Mezzasalma, M. C. Spadaro, J. Arbiol, J. Sancho-Parramon, Tailoring plasmonic resonances in Cu-Ag metal islands films, Applied Surface Science 564 (2021) 150260. doi:10.1016/j.apsusc.2021.150260.

[57] B. D. Anderson, J. B. Tracy, Nanoparticle conversion chemistry: Kirkendall effect, galvanic exchange, and anion exchange, Nanoscale 6 (2014) 12195–12216. doi:10.1039/c4nr02025a.

[58] E. González, J. Arbiol, V. F. Puntes, Carving at the Nanoscale: Sequential Galvanic Exchange and Kirkendall Growth at Room Temperature, Science 334 (2013) 1377–1380. doi:10.1126/science.1212822.

[59] J. Zhou, T. Yang, W. He, Z. Y. Pana, C. Z. Huang, A galvanic exchange process visualized on single silver nanoparticles via dark-field microscopy imaging, Nanoscale 10 (2018) 12805–12812. doi:10.1039/C8NR01879K.

[60] X. Xia, Y. Wang, A. Ruditskiy, Y. Xia, 25th Anniversary Article: Galvanic Replacement: A Simple and Versatile Route to Hollow Nanostruc-

tures with Tunable and Well-Controlled Properties, Advanced Materials 25 (2013) 6313–6333. doi:10.1002/adma.201302820.

[61] V. J. Keast, Atmospheric Corrosion of Silver and Silver Nanoparticles, Corrosion and Materials Degradation 3 (2022) 221–234. doi:10.3390/cmd3020013.

[62] Y. Sun, Y. Xia, Mechanistic Study on the Replacement Reaction between Silver Nanostructures and Chloroauric Acid in Aqueous Medium, Journal of American Chemical Society 126 (2004) 3892–3901. doi:10.1021/ja039734c.

[63] Y.-H. Chien, M.-F. Tsai, V. Shanmugam, K. Sardar, C.-L. Huang, C.-S. Yeh, Escape from the destruction of the galvanic replacement reaction for solid –> hollow –> solid conversion process in one pot reaction, Nanoscale 5 (2013) 3863–3871. doi:10.1039/C3NR00100H.

[64] P. A. Turner, H. C. Theuerer, K. L. Tai, Interdiffusion between Films of Gold and Silver, Journal of Vacuum Science and Technology 6 (1969) 650. doi:10.1116/1.1315718.

[65] G. Guisbiers, L. Buchaillot, Size and shape effects on creep and diffusion at the nanoscale, Nanotechnology 19 (2008) 435701. doi:10.1088/0957-4484/19/43/435701.

[66] D. Das, P. Chatterjee, I. Manna, S. K. Pabi, A measure of enhanced diffusion kinetics in mechanical alloying of Cu-18 at. % Al by planetary ball milling, Scripta Materialia 41 (1999) 650. doi:10.1016/S1359-6462(99)00220-1.

[67] J. Yang, J. Y. Lee, H.-P. Too, Core-shell ag-au nanoparticles from replacement reaction in organic medium, Journal of Physical Chemistry B 109 (2005) 19208–19212. doi:10.1021/jp052242x.

[68] D. M. Mott, D. T. N. Anh, P. Singh, C. Shankar, S. Maenosono, Electronic transfer as a route to increase the chemical stability in gold and silver core–shell nanoparticles, Advances in Colloid and Interface Science 185-186 (2012) 14–33. doi:10.1016/j.cis.2012.08.007.

[69] T. Xing, H. Ye, X. Hu, Z. Wang, M. Wei, L. He, L. Wu, The synthesizing approach analysis of hollow ag/au nanoparticles in replacement

reaction between silver nanoparticle and chloroauric acid, Applied Surface Science 513 (2020) 145809. doi:10.1016/j.apsusc.2020.145809.

[70] M. J. Ahemad, T. D. Le, D.-S. Kim, Y.-T. Yu, Bimetallic agau alloy@zno core-shell nanoparticles for ultra-high detection of ethanol: Potential impact of alloy composition on sensing performance, Sensors and Actuators B: Chemical 359 (2022) 131595. doi:10.1016/j.snb.2022.131595.

[71] S. Panicker, I. Ahmady, C. Han, M. Chehimi, A. Mohamed, On demand release of ionic silver from gold-silver alloy nanoparticles: fundamental antibacterial mechanisms study, Materials Today Chemistry 16 (2020) 100237. doi:10.1016/j.mtchem.2019.100237.

[72] R. S. Haider, S. Wang, Y. Gao, A. S. Malik, N. Ta, H. Li, B. Zeng, M. Dupuis, F. Fan, C. Li, Boosting photocatalytic water oxidation by surface plasmon resonance of ag_xau_{1-x} alloy nanoparticles, Nano Energy 87 (2021) 106189. doi:10.1016/j.nanoen.2021.106189.

[73] W. Albrecht, J. E. van der Hoeven, T.-S. Deng, P. E. de Jongh, A. van Blaaderen, Fully alloyed metal nanorods with highly tunable properties, Nanoscale 9 (2017) 2845–2851. doi:10.1039/C6NR08484B.

[74] Y. Ni, C. Kan, L. He, X. Zhu, M. Jiang, D. Shi, Alloyed au-ag nanorods with desired plasmonic properties and stability in harsh environments, Photonics Research 7 (2019) 558–565. doi:10.1364/PRJ.7.000558.

[75] N. Wiriyakun, K. Pankhlueab, S. Boonrungsiman, R. Laocharoensuk, Site-Selective Controlled Dealloying Process of Gold-silver Nanowire Array: a Simple Approach towards Long-Term Stability and Sensitivity Improvement of SERS Substrate, Scientific Reports 6 (2016) 39115. doi:10.1038/srep39115.

[76] B. Sharma, R. R. Frontiera, A.-I. Henry, E. Ringe, R. P. Van Duyne, SERS: Materials, applications, and future, Materials Today 15 (2012) 16–25. doi:10.1016/S1369-7021(12)70017-2.

[77] T. Vosgröne, A. J. Meixner, Surface and resonance enhanced micro-Raman spectroscopy of xanthene dyes at the single-molecule level, Journal of Luminescence 107 (2004) 13–20. doi:10.1016/j.jlumin.2003.12.041.

[78] Q. Zhou, X. Li, Q. Fan, x. Zhang, J. Zheng, Charge transfer between metal nanoparticles interconnected with a functionalized molecule probed by surface-enhanced Raman spectroscopy, Angewandte Chemie International Edition 45 (2006) 3970–3973. doi:10.1002/anie.200504419.

[79] K. Uetsuki, P. Verma, T.-A. Yano, Y. Saito, T. Ichimura, S. Kawata, When the signal is not from the original molecule to be detected: chemical transformation of para-aminothiophenol on Ag during the SERS measurement, Journal of the American chemical Society Communications 132 (2010) 9244–9246. doi:10.1021/ja101107z.

[80] M. Kang, J.-J. Kim, Y.-J. Oh, S.-G. Park, K.-H. Jeong, A Deformable Nanoplasmonic Membrane Reveals Universal Correlations Between Plasmon Resonance and Surface Enhanced Raman Scattering, Advanced Materials 26 (2014) 4510–4514. doi:10.1002/adma.201305950.

[81] P. L. Stiles, J. A. Dieringer, N. C. Shah, R. P. V. Duyne, Surface-enhanced raman spectroscopy, Annual Review of Analytical Chemistry 1 (2008) 601–626. doi:10.1146/annurev.anchem.1.031207.112814.

[82] M. Bubaš, J. S. Parramon, DFT-Based Approach Enables Deliberate Tuning of Alloy Nanostructure Plasmonic Properties, Journal of Physical Chemistry C 125 (2021) 24032–24042. doi:10.1021/acs.jpcc.1c05910.

[83] J. M. McLellan, A. Siekkinen, J. Chen, Y. Xia, Comparison of the surface-enhanced raman scattering on sharp and truncated silver nanocubes, Chemical Physics Letters 427 (2006) 122–126. doi:10.1016/j.cplett.2006.05.111.

[84] C. Wang, B. Liu, X. Dou, Silver nanotriangles-loaded filter paper for ultrasensitive sers detection application benefited by interspacing of sharp edges, Sensors and Actuators B: Chemical 231 (2016) 357–364. doi:10.1016/j.snb.2016.03.030.

[85] I. Dzięcielewski, J. Smalc-Koziorowska, M. Bańkowska, T. Sochacki, A. Khachapuridze, J. Weyher, Impact of temperature-induced coalescence on SERS properties of Au nanoparticles deposited on GaN nano-columns, Applied Surface Science 378 (2016) 30–36. doi:10.1016/j.apsusc.2016.03.200.

[86] A. V. Girão, P. C. Pinheiro, M. Ferro, T. Trindade, Tailoring gold and silver colloidal bimetallic nanoalloys towards SERS detection of rhodamine 6G, RSC Advances 7 (2017) 15944–15951. doi:10.1039/C7RA00685C.

[87] Y. Qin, Y. Wu, B. Wang, J. Wang, W. Yao, Facile synthesis of Ag@Au core-satellite nanowires for highly sensitive SERS detection for tropane alkaloids, Journal of Alloys and Compounds 884 (2021) 161053. doi:10.1016/j.jallcom.2021.161053.

[88] A. Jiao, X. Dong, H. Zhang, L. Xu, Y. Tian, X. Liu, M. Chen, Construction of pure worm-like AuAg nanochains for ultrasensitive SERS detection of pesticide residues on apple surfaces, Spectrochimica Acta Part A: Molecular and Biomolecular Spectroscopy 209 (2019) 241–247. doi:10.1016/j.saa.2018.10.051.

[89] J. Zhao, L. Long, G. Weng, J. Li, J. Zhu, J.-W. Zhao, Multibranch Au/Ag bimetallic core–shell–satellite nanoparticles as a versatile SERS substrate: the effect of Au branches in a mesoporous silica interlayer, Journal of Materials Chemistry C 5 (2017) 12678–12687. doi:10.1039/C7TC03788K.

[90] I. Haidar, A. Day, U. Martino, A. Chevillot-Biraud, N. Félidj, L. Boubekeur-Lecaque, Bottom-up assembly of Au@Ag plasmonic nanocrystals: Issues to be addressed to achieve a good SERS substrate, Applied Materials Today 15 (2019) 462–471. doi:10.1016/j.apmt.2019.02.015.

[91] D. Xu, H. Jiang, W. Yang, S. Zhang, J. Chen, SERS effect of Rhodamine 6G molecular probe on AgAu alloy nanowire arrays by a solid-state ionics method, Physica E: Low-dimensional Systems and Nanostructures 102 (2018) 132–136. doi:10.1016/j.physe.2018.05.005.

[92] H. Li, H. Liu, Y. Qin, Y. Mu, X. Fang, T. Zhai, X. Zhang, Gold-Stabilized Gold–Silver Alloy Nanostructures as High-Performance SERS Substrate, Plasmonics 15 (2020) 2027–2032. doi:10.1007/s11468-020-01229-0.

[93] R. Gessner, P. Rösch, W. Kiefer, J. Popp, Raman spectroscopy investigation of biological materials by use of etched and silver coated glass fiber tips, Biopolymers 67 (2002) 327–330. doi:10.1002/bip.10090.

[94] J. Kwak, W. Lee, J.-B. Kim, S.-I. Bae, K.-H. Jeong, Fiber-optic plasmonic probe with nanogap-rich Au nanoislands for on-site surface-enhanced Raman spectroscopy using repeated solid-state dewetting, Journal of Biomedical Optics 24 (2019) 037001. doi:10.1117/1.JBO.24.3.037001.

[95] Y. Ran, P. Strobbia, V. Cupil-Garcia, T. Vo-Dinh, Fiber-optrode SERS probes using plasmonic silver-coated gold nanostars, Sensors and Actuators B: Chemical 287 (2019) 95–101. doi:10.1016/j.snb.2019.01.167.

[96] A. Genç, J. Patarroyo, J. Sancho-Parramon, N. G. Bastús, V. Puntes, J. Arbiol, Hollow metal nanostructures for enhanced plasmonics: synthesis, local plasmonic properties and applications, Nanophotonics 6 (1) (2017) 193–213. doi:10.1515/nanoph-2016-0124.